Rare Metal Materials and Engineering
Volume 48, Issue 9, September 2019
Available online at www.rmme.ac.cn

Science Press

Cite this article as: Rare Metal Materials and Engineering, 2019, 48(9): 2759-2767.

ARTICLE

Effects of Casting Parameters on Macrosegregation in 2024 Alloy During Direct-chill Casting Based on Numerical Simulation

Luo Haijun[1], Jie Wanqi[1], Gao Zhiming[1], Zheng Yongjian[2]

[1] State Key Laboratory of Solidification Processing, Northwestern Polytechnical University, Xi'an 710072, China; [2] University of Leoben, Leoben A-8700, Austria

Abstract: The extended continuum mixture model considering the floating grain motion was applied to calculate the macrosegregation of large-size billet of 2024 aluminum alloy during direct-chill (DC) casting. Transport equations of mass, momentum, species and heat were solved simultaneously with the Scheil-Gulliver micro-model. The effects of casting parameters (billet size, casting speed, casting temperature and intensity of secondary cooling zone) on macrosegregation were calculated in nine cases. Influence of casting parameters on the transport mechanisms for macrosegregation formation was discussed. The results demonstrate that the processing parameters directly affect the shape and dimension of the sump, thereby affecting the final segregation patterns. The billet size and casting speed play the most important roles. A larger billet size usually means a slower cooling rate and a deeper and wider sump, which results in severe segregation in the billet center. The sump depth dramatically increases with the increase of the casting speed. Therefore, higher casting speed promotes greater macrosegregation. Nevertheless, the sump depth increases slightly with increasing the casting temperature.

Key words: casting parameters; direct-chill casting; macrosegregation; numerical simulation; 2024 alloy

Direct-chill casting has been widely used for the commercial production of extrusion billets of wrought aluminum alloys since 1930s. One of the major defects in this process is macrosegregation. Macrosegregation is caused by solute transport due to the flow of segregated liquid in the mushy zone and the motion of free grains. Comprehensive reviews on macrosegregation are given in Ref.[1-5].

The modeling for macrosegregation in DC casting has been investigated in recent decades. In the last century, Reddy and Beckerman [6] studied the effects of mushy permeability, thermosolutal convection and solidification contraction on the macrosegregation pattern in DC casting of an Al-4.5wt%Cu round ingot. They found that centerline segregation can be positive or negative, depending upon the grain density and permeability of the mush. Then, Du et al [7] studied the macrosegregation of a ternary Al-Cu-Mg alloy by CALPHAD software, and solidification path was described using a modified mapping technique [8]. The semi-quantitative results showed that the contribution of each solute element to the solutal buoyancy affects the final segregation pattern and an overestimation of centerline segregation was obtained, where the model did not take the possible contribution of floating grains and exudation into account. Vusanovic [9] applied a non-equilibrium microsegregation model in a horizontal DC casting ternary Al-4.5wt%Cu-1.0wt%Mg alloy. They found that the copper exhibits less segregation compared to Al-Cu alloy, while magnesium has a similar segregation profile but is less pronounced. Zaloznik et al [10] studied the macrosegregation formation in a 7449 alloy industrial scale slab during direct-chill casting using a multi-scale two-phase solidification model. They analyzed the individual and combined effects of shrinkage, natural convection, and grain motion on the sump profile and macrosegregation formation. Recently, Ellingsen et al [11] modeled the macrosegregation in a 5182 aluminum

Received date: August 05, 2018
Foundation item: National Natural Science Foundation of China (51420105005); National Key Research and Development Program of China (2016YFF0101301)
Corresponding author: Jie Wanqi, Professor, State Key Laboratory of Solidification Processing, Northwestern Polytechnical University, Xi'an 710072, P. R. China, Tel: 0086-29-88495414, E-mail: jwq@nwpu.edu.cn

alloy, accounting for secondary phase formation. The results demonstrated that the effect of secondary phase precipitation on macrosegregation formation is caused by shrinkage induced flow.

Some studies on parameterization of macrosegregation have been done over the past years. Dorward and Beerntsen [12] studied 2024 alloy billets with varying parameters, including casting speeds, melt temperatures and mold water flow rates. Their results showed that higher casting speed promotes deeper liquid metal sump due to the collection of coarse solute-depleted isothermal dendrites in the center of the ingot, resulting in negative macrosegregation in the center. The cooling water flow also exerts important effect. The melt superheat increased the depth of sump slightly, resulting in the formation of solute-depleted primaries. Eskin et al [13] presented an experimental investigation about the dependence of macrosegregation and structure on process parameters. They found that decreasing the casting speed and the water-flow rate produce less macrosegregation. The main parameters influencing structure and macrosegregation during direct-chill casting are the depth of the liquid pool, the sump and the flow pattern in the slurry region. Du et al [14] studied the effect of ramping casting speed and casting temperature on temperature distribution and melt flow patterns of DC casting billet. Their results showed that the lower position of the liquid isotherm will produce a more severe melt flow towards the surface and a deeper penetration into mushy zone at a higher casting temperature. Založnik, and Šarler[15] estimated the influence of casting parameters on macrosegregation in DC casting of Al-5.25wt%Cu. Their results showed the trends caused by variation of the parameters which influence the macrosegregation pattern through their direct impact on the thermosolutal convection flow in the liquid pool, the shape and thickness of the mushy zone.

We extended the continuum mixture model for binary alloys to the multi-component system, which was successfully used for the macrosegregation predication. Based on the modeling method, the present paper studied the effects of casting parameters, such as billet size, casting speed, casting temperature and intensity of secondary cooling zone, on the macrosegregation of 2024 aluminum alloy billet in large size during DC casting.

1 Model Description

Based on the continuum mixture model with free floating solid particles formulated by Vreeman et al [16], separate and distinct mixture momentum equations are employed to account for momentum transfer in two-phase regions. The macroscopic transport equations for heat, mass, momentum and species are solved.

For the solidification process of a multicomponent alloy during DC casting, the Gulliver-Scheil model was used to calculate the solidification path according to the phase diagrams, which were formulated as simple, approximate, and analytical expressions[11, 17, 18]. This stand-alone microscopic module for the calculation of the solidification path of Al-Mg-Cu alloys in the Al-rich corner of the phase diagram was solved simultaneously with macroscopic transport equations[19].

Modeling of the fluid flow behavior in different regions was carried by viscosity and permeability functions [14], as given in Table 1. When the solid fraction f_s is less than f_{sco} (coherent solid fraction), the permeability is infinite. In regions with the solid fraction f_s larger than f_{sco}, the permeability is a function of solid fraction through the Blake-Kozeny-Carman relation. The permeability coefficient K_0=2.0×10^{-11} m^2 was used. This value is based on a dendrite arm spacing of 60 μm, which was measured in the experiment[12].

2 Solution Methods

2.1 Numerical solution procedures

The macroscopic transport equations were solved by computational fluid dynamics software FLUENT, which discretized all equations with the finite volume method. The scheme of pressure-speed coupling used SIMPLE algorithm. The second-order upwind scheme was adopted to deal with the convection term of momentum and species equations, and the first-order upwind scheme was for energy equation. Source terms, permeability model and complex boundary conditions were hooked to FLUENT model by UDFs. The whole computational domain in axisymmetric geometry was divided into quadrilateral mesh of 1 mm×1 mm. A grid of 200×1100 control volume cells were used in basic case 2 and varied accordingly with other cases. For each time-step, up to 40 iterations and 0.001 s for time step were adopted to get good convergence.

2.2 Thermophysical parameters

The 2024 alloy contains three main alloying solute elements, including Cu, Mg and Mn (Table 2). Since the partition coefficient of manganese is approximately 1, the segregation of manganese is ignored, and the alloy is simplified to a ternary system with the composition of Al-4.5wt%Cu-1.5wt%Mg [20].

Alternatively, manganese is the transition element with a strong bonding capacity, which can increase the bonding force between atoms and prevent atomic diffusion. Hence, it would primarily influence the diffusion coefficients of Cu and Mg.

Table 1 Viscosity and permeability in different regions

Region	Solid fraction, f_s	Mixture viscosity, μ_m	Permeability, K
Liquid	0	μ_l	∞
Slurry	$0<f_s\leqslant f_{sco}$	$\mu_m=\mu_l(1.0-\frac{f_s}{f_{scr}})^{-1.5}$	∞
Mushy	$f_{sco}<f_s\leqslant 1$	$\mu_m=\mu_l(1.0-\frac{f_s}{f_{scr}})^{-1.5}$	$K=K_0\frac{(1-f_s)^2}{f_s^2}$

Table 2 Nominal composition of AA2024 (wt%)

Cu	Mg	Mn	Fe/Si	Cr	Ti	Al
3.8~4.9	1.2~1.8	0.3~0.9	≤ 0.50	≤ 0.10	0.15	Bal.

However, in the Gulliver-Scheil model, we assumed that no diffusion occurs in solid phases and that infinite fast diffusion occurs in the liquid. Furthermore, thermophysical parameters depend mainly on the temperature. Thus, its effect on thermophysical parameters can be reasonably neglected.

For the sake of simplicity, the values of specific heat and thermal conductivity were reduced to constant. The relationship of density of liquid phase, namely $\rho_l = \rho_l(T, C_l) = \rho_0\left[1-\beta_T(T-T_0)-\beta_c(C-C_0)\right]$, was only applied into momentum equations. The thermophysical parameters are listed in Table 3, which are obtained mainly from Ref.[7, 9].

2.3 Geometric model and boundary conditions

The 2D axisymmetric geometry model and mesh (grid precision 1 mm×1 mm) used in this work are shown in Fig.1. The basic ingot with diameter of 400 mm and length of 950 mm was simulated. 50 mm in width was set for the inlet and hot-top, 100 mm in length was for the water-cooled mold, and 950 mm was for the water film. The boundary conditions are also given. Free surface, hot top and symmetry axis are treated as the static adiabatic wall. For the mold-casting interface, the heat transfer coefficient h_{mold} is treated as follows:

$$h_{mold} = h_{con}\cdot(1-f_s) + h_{air}\cdot f_s \quad (1)$$

where h_{con} is 1500 W/(m$^2\cdot$K), and h_{air} is 150 W/(m$^2\cdot$K). In the secondary cooling zone, the following Weckman-Niessen correlation [21] is used for heat transfer coefficient:

Table 3 Thermophysical parameters

Parameters	Value
Liquid density, ρ_l /kg·m^{-3}	2606
Solid density, ρ_s /kg·m^{-3}	2750
Liquid specific heat, c_l /J·(kg·K)$^{-1}$	1054
Solid specific heat, c_s /J·(kg·K)$^{-1}$	958
Liquid thermal conductivity, k_l /W·(m·K)$^{-1}$	95.0
Solid thermal conductivity, k_s /W·(m·K)$^{-1}$	180
Liquid diffusion coefficient, $D_l^{Cu/Mg}$ /m^2·s^{-1}	5.0×10^{-9}/2.0×10^{-8}
Liquid viscosity, μ_l /kg·(m·s)$^{-1}$	0.0013
Average solid viscosity, $\overline{\mu}_s$ /kg·(m·s)$^{-1}$	4.96 μ_l
Solutal expansion coefficient, $\beta_l^{Cu/Mg}$ /K^{-1}	-0.73/0.5
Thermal expansion coefficient, β_T /K^{-1}	1.17×10^{-4}
Melting point of Al, T_{melt} /K	933.5
Eutectic temperature, T_{Eut} /K	781
Eutectic composition, $C_{Eut}^{Cu/Mg}$ /wt%	44.8/17.2
Equilibrium partition coefficient, k_p (Cu/Mg)	0.12/0.43
Reference temperature, T_0 /K	884
Reference concentration, $C_0^{Cu/Mg}$ (Cu/Mg)	4.5/1.5
Permeability constant, K_0 /m^2	2.0×10^{-11}

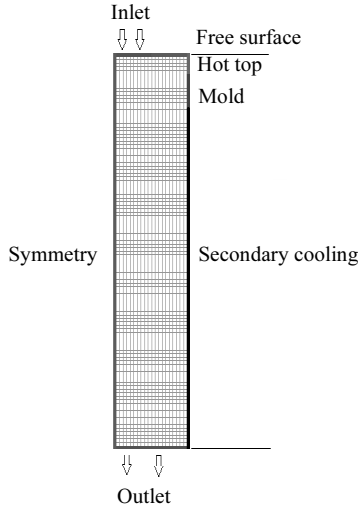

Fig.1 Schematic diagram of direct-chill casting and geometry mesh

$$h_{sec}(T) = [-167000 + 352(T - T_{water})]\cdot\left(\frac{Q_{water}}{P}\right)^{1/3} + 20.8\left(\frac{(T - T_{saturation})^3}{T - T_{water}}\right) \quad (2)$$

where Q_{water} is water flow rate, P is width of water film, $T_{saturation}$ is saturation temperature of water, and T_{water} is temperature of the cooling water. Moreover, no-slip boundary conditions are applied to the walls.

3 Results and Discussion

9 cases were simulated in this paper. Case 1, case 2 and case 3 are for different billet sizes (d); case 4, case 2 and case 5 are for different casting speeds (v_{cast}); case 6, case 2 and case 7 are for different casting temperatures (T_{cast}); case 8, case 2 and case 9 are for different intensities of secondary cooling zone (Q_{water}). Case 2 is the basic case. 4 most important processing parameters affecting macrosegregation and more details are illustrated in Table 4.

Fig.2 shows the contours of temperature, velocity and segregation for the basic case 2 at the steady state. The hot melt from the inlet flows almost horizontally towards the surface, due to the suck effect of melt solidification quenched by the water cooling mold, as shown in Fig.2b. Accordingly, the positive segregation occurs on the surface due to the inverse segregation. This flow then deflects because of the block of the rigid solid matrix and moves along the interface of the rigid solid and the slurry region towards the centerline. Hence, the clock-wise recirculation is established.

Simultaneously, the negative segregation in the subsurface is produced by this thermosolutal flow, which washes the solute-rich liquid out of the mush. This contribution together with the shrinkage-induced flow which carries the solute-rich liquid from center to surface create the positive segregation in

Table 4 Cases studied in this work

Case	d/mm	v_{cast}/mm·min^{-1}	T_{cast}/K	Q_{water}/L·min^{-1}
1	200	63.5	991	250
2	400	63.5	991	250
3	600	63.5	991	250
4	400	32	991	250
5	400	127	991	250
6	400	63.5	951	250
7	400	63.5	1031	250
8	400	63.5	991	125
9	400	63.5	991	375

the middle radius. Both the shrinkage-induced flow and the floating grains are prone to produce a negative effect, causing the negative segregation in centerline. The predicted segregation in case 2 and the experimental results measured by Dorward et al[12] are compared in Fig.2c. They are consistent with each other in general but the extent of the negative or positive segregation in experiments is much more severe than that in case 2. The reason can be attributed to three aspects[19]. First, the 2024 aluminum alloys used in experiment have more than 3 components and impurities. Hence, it will lead to a certain extent of grain refinement. This will change the resistance to flow through the solid network (mushy zone), reducing the permeability in the mushy zone and lowering the coherency temperature. The lower permeability will impede the flow induced by shrinkage, narrow the rigid mushy zone, and prevent the penetration of convective flows into the rigid mushy zone. Meanwhile, the lower coherency temperature means that the convective flow and grain floating have more transport opportunities in a wider slurry zone. Secondly, as well known, the dendrite structure in large billets undergoes a columnar to equiaxed transition around the mid-radius, caused by the fragmentation of the columnar dendrites. This will produce a much larger slurry region and packing fraction. In our calculation, as suggested by Ref.[22], the packing fraction is set to 0.3, which is not a very accurate value in the actual alloy. The lower composition at the mid-radius in simulation indicates that the packing fraction should be set to a slightly larger value, since the degree of segregation increases with increasing the packing fraction. Thirdly, the boundary conditions used in calculation are not exactly the same as that in the experiment.

3.1 Effect of billet size

Fig.3 shows the distribution of temperature and flow fields under different billet sizes. It can be easily seen that the patterns of thermosolutal flow in case 1 and case 3 are similar to those in case 2.

Fig.4a shows that the position of liquidus and solidus isotherms moves downward significantly in the center with increasing the size of the billet, and the slope of the sump is also increased. The former provides more opportunity for the floating grains to settle. The latter influences the segregation induced by shrinkage, according to Eq.(3) [23].

$$L_h = 0.78C_0L_m\beta(\sin 2\alpha)/2 \quad (3)$$

where L_m is the vertical dimension of the mushy zone, β is the volumetric shrinkage, α is the angle between the tangent and the coherency isotherm and the horizon. The value of $(dL_h/dR)/C_0$ denotes the relative segregation. Hence, both of them are prone to promote more negative segregation in the larger billet center.

Fig.4d shows the segregation in the radial direction for different billet sizes. In these three cases, there are positive segregation in the mid-radius and surface, whereas negative segregation regions are generated in the center and subsurface. Meanwhile, the segregation increases with increasing the billet size. The reason is that macrosegregation depends mainly on the average cooling rate in these cases. Larger billet size causes the slower cooling rate, and accordingly severer segregation in the billet. The average cooling rate is about 10 K/s for case

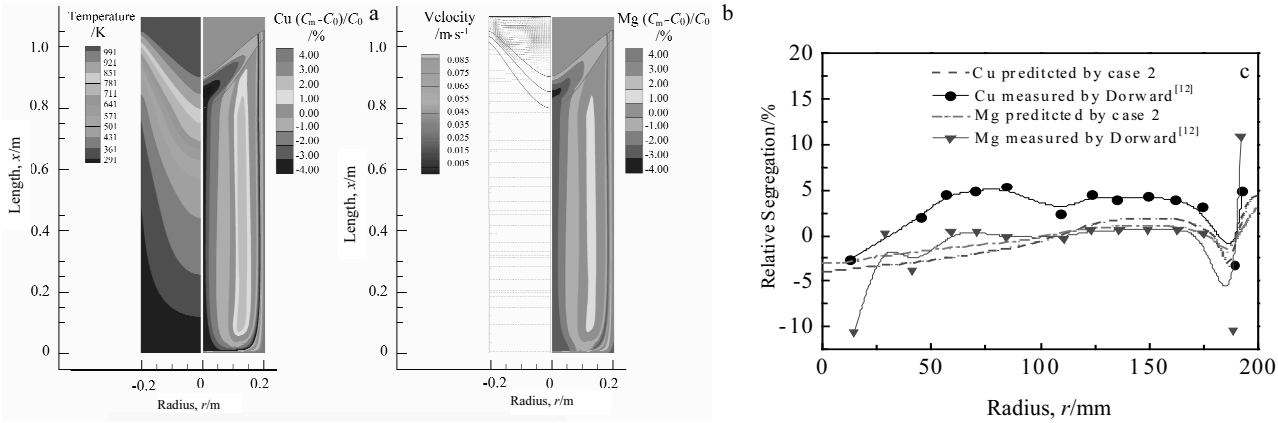

Fig.2 Temperature, flow fields and segregation profiles in case 2: (a) temperature field and Cu relative segregation, (b) flow field and Mg relative segregation, and (c) comparison of segregation ($(C-C_0)/C_0$) and experimental results measured by Dorward [12]

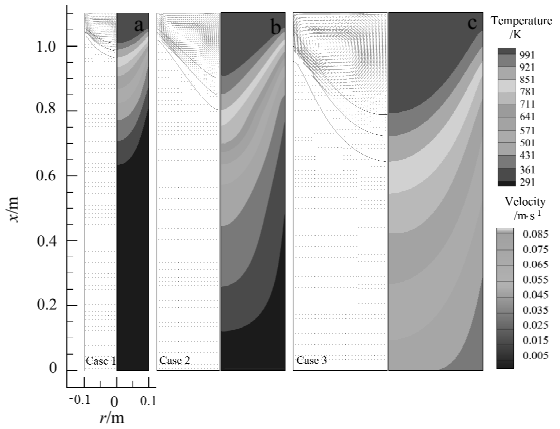

Fig.3 Distribution of temperature and flow fields under different billet sizes: (a) d=200 mm, (b) d=400 mm, and (c) d=600 mm

1, 5 K/s for case 2, and 1.5 K/s for case 3, as shown in Fig.4c.

In addition, the shape and dimension of the sump with variant billet sizes (Fig.4a) indicate that the lengths of the sump for three cases are 70, 208 and 365 mm, separately. These predicted results are in accordance with the values calculated by Eq.(3), as shown in Fig.4b. In particular, as the billet size is 600 mm in diameter, the values are quite close. The empirical formula [24] is described as below:

$$H = A \cdot v_{\text{cast}} \cdot R^2 / 4k_{\text{s}} \left(T_{\text{melt}} - T_{\text{surface}} \right) \quad (4)$$

where T_{melt} is melt temperature, T_{surface} is temperature of the billet surface, R is billet radius, k_{s} is thermal conductivity of solid, and A is about 9.67×10^8 in our calculation.

3.2 Effect of casting speed

The casting speed mainly affects the segregation in two ways. One is the change of the scope of the sump, which changes the thermosolutal convection and free dendrite transport. The other is the change of the slope of solidification front, which changes the shrinkage-induced segregation.

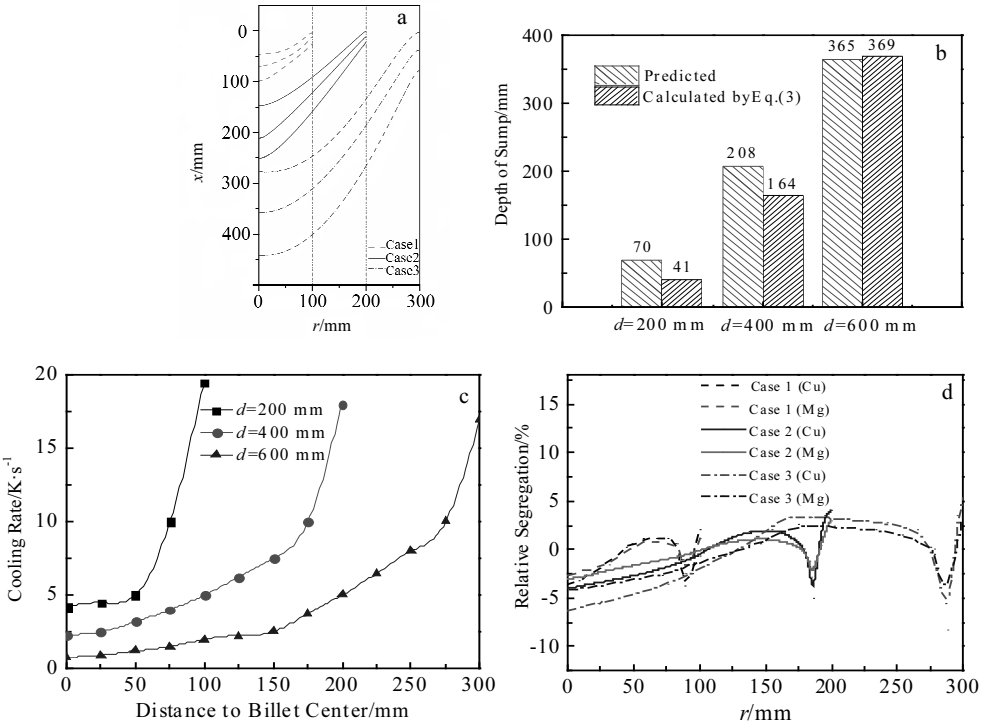

Fig.4 Comparison of segregation under different billet sizes (v_{cast}=63.5 mm/min, T_{cast}=991 K, Q_{water}=250 L/min): (a) shapes of sump, (b) predicted depth of sump and values calculated by Eq.(3), (c) cooling rates along the radial direction, and (d) relative segregation ($(C-C_0)/C_0$) profiles

Fig.5 shows the distribution of temperature and flow fields under different casting speeds. It is clear that the flow is clockwise in case 4 and 5, and the velocity of flow increases from 0.015 m/s to 0.085 m/s. The sump becomes much deeper with increasing the casting speed.

Fig.6a shows the effect of casting speed on the shape of mushy zone. It can be seen that the liquidus and solidus decrease dramatically with increasing the casting speed. Fig.6b shows that the predicted depths of the sump for three cases are125, 208 and 282 mm, separately. The segregation patterns in case 2 and 5 are similar (Fig.6c).

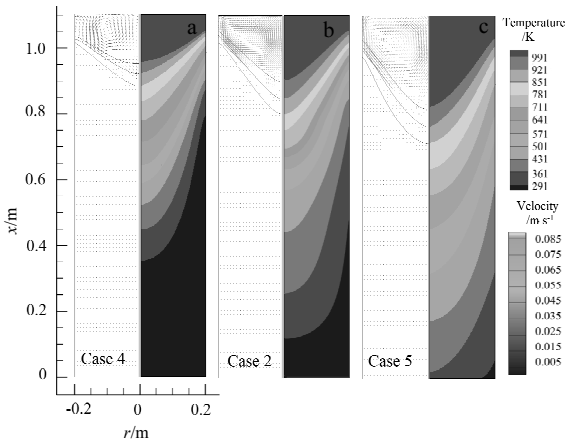

Fig.5 Distribution of temperature and flow fields under different casting speeds: (a) v_{cast}=32 mm/min, (b) v_{cast}=63.5 mm/min, and (c) v_{cast}=127 mm/min

In case 4, where the casting speed is 32 mm/min, the segregation is dramatically different. In this situation, the sump is shallow and the slope is gentle with the value of 30º, compared with other two cases (45º of case 2 and 60º of case 5). Therefore, the positive segregation is generated in the center where the contribution to the positive segregation induced by thermosolutal convection dominates over the shrinkage-induced negative segregation. Meanwhile, the negative effect of the floating grains on the center segregation is ignored. This is also in accordance with the normal segregation criterion [25]. If $v_{cast} \cdot d / a \le 1$, where d is the billet diameter and α is an alloy-dependent constant, about 16 000, the experimental result of Dorward et al [12] also supports this results. It should be noted that this criterion is a function of the size of the billet and the casting speed. Case 2 and 5 are in verse situations, and the extent of segregation in case 2 is about 25% less than that in case 5.

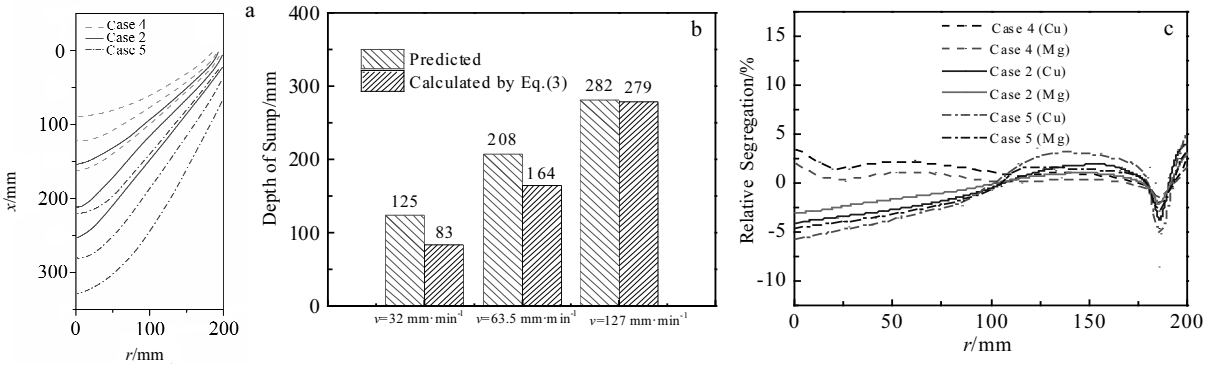

Fig.6 Comparison of segregation under different casting speeds (d=400 mm, T_{cast}=991 K, Q_{water}=250 L/min): (a) shapes of sump, (b) predicted depths and the values calculated by Eq.(3), and (c) relative segregation ($(C-C_0)/C_0$) profiles

3.3 Effect of casting temperature

Fig.7 shows the distribution of temperature and flow fields under different casting temperatures. There are similar situations for the flow patterns in case 6, 2 and 7. The velocity of flow increases slightly with increasing the casting temperatures.

Fig.8a shows that the position of the mushy zone shifts slightly downward with increasing the casting temperature. Hence, the increase of the melt temperature has very few effects on the shape and dimension of the mushy zone, but affects the liquidus isotherms to a certain extent. The melt temperature varies from 951 K to 1031 K, accordingly the superheat of 40 °C for case 6, 80 °C for case 2, and 120 °C for case 7. Fig.8b shows that the predicted depths of the sump for three cases are 202, 208 and 216 mm. Hence, the depth of the sump increases slightly with increasing the melt temperature.

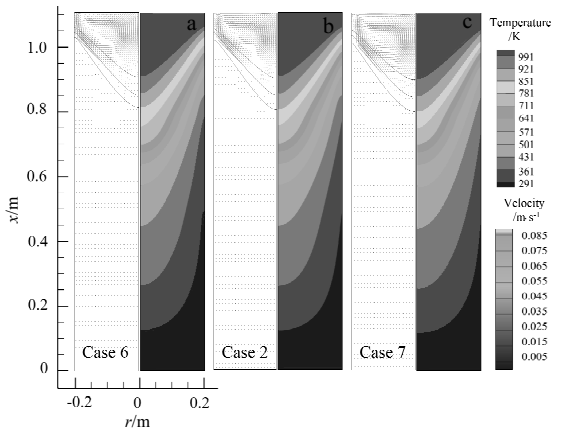

Fig.7 Distribution of temperature and flow fields under different casting temperatures: (a) T_{cast}=951 K, (b) T_{cast}=991 K, and (c) T_{cast}=1031 K

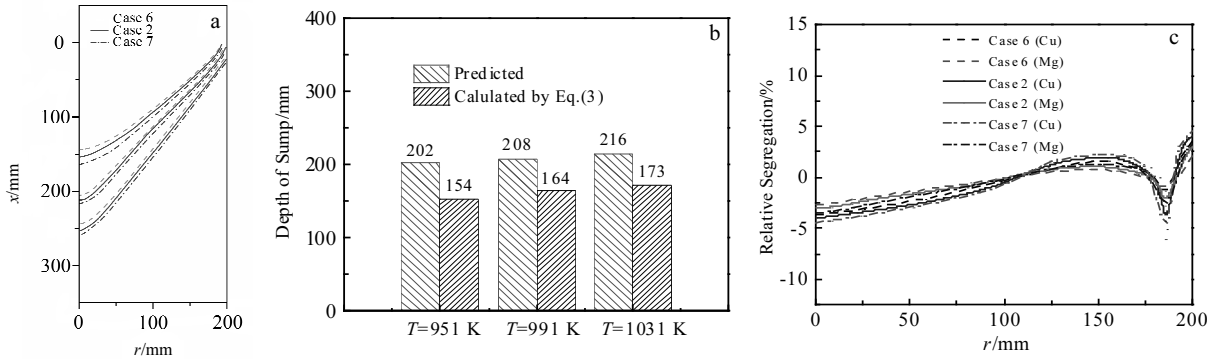

Fig.8 Comparison of segregation at different casting temperatures (d=400 mm, v_{cast}=63.5 mm/min, Q_{water}=250 L/min): (a) shapes of sump, (b) predicted depths and the values calculated by Eq.(3), and (c) relative segregation ($(C-C_0)/C_0$) profiles

The higher melt temperature results in a higher temperature gradient in the liquid, corresponding to the higher driving force for thermo-solutal convection and benefits the strong melt flow from the billet surface to the centerline. The melt flow will penetrate deeper into the mushy zone and bring more solute-rich liquid to the center, and cause more negative segregation in the subsurface (illustrated in Fig.7). However, the positive segregation induced by this flow is counteracted by an increased amount of floating grains caused by a higher superheat in the center. The melt superheat has little effect on the shrinkage-induced segregation because the slope of the solidification front is hardly affected by the melt temperature. Above all, only the segregation in the subsurface and surface of the billet increases to a certain extent as casting temperature increases, as shown in Fig.8c.

3.4 Effect of intensity of secondary cooling zone

The heat transfer coefficients for primary cooling in the mold and secondary cooling zone are dependent on the water flow rate [26]. This water flow rate significantly affects the intensity of secondary cooling zone, because the mold heat flux is mainly controlled by the interfacial gap and thickness of the solidifying shell.

Fig.9 shows the distribution of temperature and flow fields under different intensities of secondary cooling zone. The flow pattern in case 8 and 9 is similar to that in case 2. The velocity of flow and the positions of liquidus and solidus decrease with increasing the intensities of secondary cooling zone.

Fig.10a shows the shape of the sump with variant water flow rates. The predicted depths of the sump in three cases are 235, 208 and 186 mm, separately (Fig.10b). Case 9 with higher water flow rate has a narrower and more gentle sump. However, there is almost no change in the isotherms at the

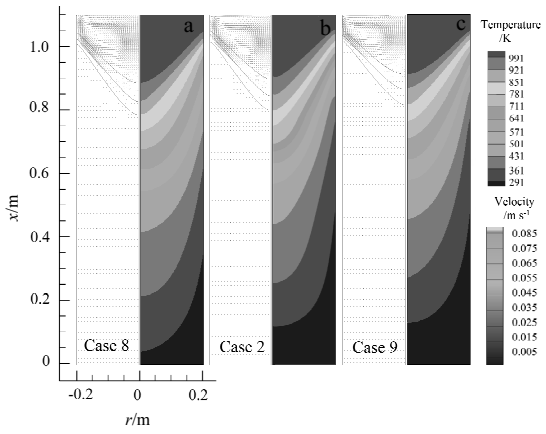

Fig.9 Distribution of temperature and flow fields under different intensities of secondary cooling zone: (a) Q_{water}=125 L/min, (b) Q_{water}=250 L/min, and (c) Q_{water}=375 L/min

periphery of the billet in the mold. The predicted results are also supported by Prasso et al [27, 28]

In these cases, the segregation induced by shrinkage will decrease the negative segregation in the center, due to the shorter length of mushy zone and the almost invariant slope of the solidification front (Eq.(4)). Furthermore, the thermo-solutal flow is restricted in narrow mushy zone and less solute-rich liquid is taken out, resulting in the alleviative segregation. In addition, the floating grains have less opportunity to accumulate in this narrow mushy zone. All in all, the segregation decreases with increasing the intensities of secondary cooling zone (Fig.10c). It is also noted that this effect is insignificant if the cooling intensity provided by water flow rate is sufficient.

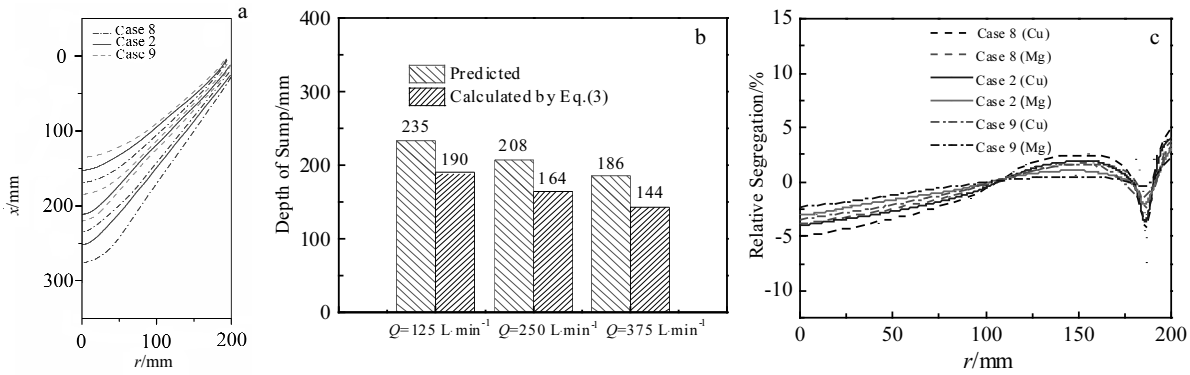

Fig.10 Comparison of segregation with different intensities of secondary cooling zone (d=400 mm, v_{cast}=63.5 mm/min, T_{cast}=991 K): (a) shapes of sump, (b) predicted depths and the values calculated by Eq.(3), and (c) relative segregation ($(C-C_0)/C_0$) profiles

4 Conclusions

1) A larger billet size usually means a slower cooling rate, a deeper and wider sump, which results in the severer segregation in the billet center. The sump magnitude exerts a stronger effect than the casting speed. The segregation increases with increasing the billet size at a given casting speed.

2) Increasing the casting speed dramatically increases the sump depth. Therefore, higher casting speed promotes a larger macrosegregation. In comparison with other casting parameters, the effects of casting speed on segregation are significant.

3) The sump depth increases slightly with increasing the casting temperature. The segregation in the subsurface and surface of the billet increases as casting temperature increases, but there is no remarkable effect on the rest of the billet.

4) A higher water flow rate produces a narrower and flatter sump. The thermo-solutal flow and floating grain motion as well as the shrinkage-induced flow are restricted. Therefore, segregation decreases with increasing the intensity of secondary cooling zone.

References

1 Flemings M C. *ISIJ Int*[J], 2000, 40(9): 838
2 Beckermann C. *Int Mater Rev*[J], 2002, 47(5): 243
3 Nadella R, Eskin D G, Du Q *et al*. *Prog Mater Sci*[J], 2008, 53(3): 421
4 Pickering E J. *ISIJ Int*[J], 2013, 53(6): 935
5 Grandfield J F, Eskin D G, Bainbridge I. *Direct-chill Casting of Light Alloys*[M]. New Jersey: John Wiley & Sons, Inc, 2013: 331
6 Reddy A V, Beckermann N C. *Metall Mater Trans B*[J], 1997, 28(3): 479
7 Du Q, Eskin D G, Katgerman L. *Metall Mater Trans A*[J], 2007, 38(1): 180
8 Dor X, Combeau H, Rappaz M. *Acta Mater*[J], 2000, 48(15): 3951
9 Vusanovic I. *Int J Cast Met Res*[J], 2009, 22(1): 314
10 Založnik M, Kumar A, Combeau H *et al*. *Adv Eng Mater*[J], 2011, 13(7): 570
11 Ellingsen K, M'hamdi M, Tveito K *et al*. *TMS Light Metals*[J], 2014, 188(6): 861
12 Dorward R C, Beerntsen D J. *Light Metals*[J], 1990(3): 919
13 Eskin D G, Zuidema J, Savran V I *et al*. *Mater Sci Eng A*[J], 2004, 384(1-2): 232
14 Du Q, Eskin D G, Katgerman L. *Mater Sci Eng A*[J], 2005, 413-414(6): 144
15 Založnik M, Šarler B. *Mater Sci Eng A*[J], 2005, 413-414: 85
16 Vreeman C J, Krane M J M, Incropera F P. *Int J Heat Mass Transfer*[J], 2000, 43(5): 687
17 Ellingsen K, Mortensen D, Hamdi M M. *IOP Conf Ser Mater Sci Eng*[J], 2015, 84(1): 12
18 Ellingsen K, Dons A L, M'hamdi M *et al*. *Int J Cast Met Res*[J], 2009, 22(1-4): 220
19 Luo H J, Jie W Q, Gao Z M *et al*. *Trans Nonferrous Met Soc China*[J], 2018, 28(5): 1005
20 Nadella R, Eskin D G, Katgerman L. *Metall Mater Trans A*[J], 2007, 39(2): 450
21 Weckman D C, Niessen P. *Metall Mater Trans B*[J], 1982, 13(4): 593
22 Vreeman C J, Krane M J M, Incropera F P. *Int J Heat Mass Transfer*[J], 2000, 43(5): 687
23 Eskin D G, Du Q, Katgerman L. *Scr Mater*[J], 2006, 55(8): 715
24 Eskin D G. *Physical Metallurgy of Direct Chill Casting of Aluminum Alloys*[M]. Boca Raton: CRC Press, 2008: 81
25 Livanov V A, Gabidullin R M, Shipilov V S. *Continuous Casting of Aluminum*[M]. Moscow: Metallurgiya, 1977: 50
26 Sengupta J, Thomas B G, Wells M A. *Metall Mater Trans A*[J], 2005, 36(1): 187
27 Prasso D C, Evans J W, Wilson I J. *Metall Mater Trans B*[J], 1995, 26(1): 1243
28 Prasso D C, Evans J W, Wilson I J. *Metall Mater Trans B*[J], 1995, 26(1): 1281

铸造参数对 2024 铝合金半连铸过程中宏观偏析影响的数值模拟

罗海军[1]，介万奇[1]，高志明[1]，郑永健[2]

(1. 西北工业大学 凝固技术国家重点实验室，陕西 西安 710072)

(2. University of Leoben, Leoben A-8700, Austria)

摘　要：采用考虑了浮游晶运动的拓展连续模型计算大尺寸 2024 铝合金半连铸铸锭的宏观偏析。模型中宏观的传质、传热、动量传输方程与 Scheil-Gulliver 微观凝固模型相互耦合。通过 9 个算例计算铸造参数（铸锭尺寸、铸造速度、浇注温度以及二冷区冷却强度）对宏观偏析的影响，并讨论了铸造参数对形成宏观偏析传输机制的影响。结果表明，铸造参数直接影响熔池的形状和尺寸进而影响最终偏析形态。其中，铸锭尺寸和铸造速度是最主要的影响因素。更大的铸锭尺寸通常意味着更慢的冷却速度，以及更深和更宽的熔池，从而导致铸锭中心更严重的宏观偏析。增加铸造速度则将显著地增加熔池的深度，因而更大的铸造速度将导致更严重的宏观偏析。而熔池的深度随浇注温度的增加仅轻微增加，故浇注温度对宏观偏析的影响不如前二者敏感。

关键词：铸造参数；半连铸；宏观偏析；数值模拟；2024铝合金

作者简介：罗海军，男，1985 年生，博士生，西北工业大学材料学院，陕西 西安 710072，电话：029-88495414，E-mail: lhj273@163.com